Metals and Materials International
https://doi.org/10.1007/s12540-024-01636-6

A Practical Inverse Identification of Johnson–Cook Parameters at Intermediate Strain Rates Using Split Hopkinson Pressure Bar Test

Yeong-Min Jeong[1,2] · Seojun Hong[1] · Jung Yun Won[1] · Chanyang Kim[3] · Myoung-Gyu Lee[1]

Received: 4 November 2023 / Accepted: 16 January 2024

Abstract
A practical inverse method based on the hybrid experiment-finite element (FE) simulation is proposed for identifying strain rate sensitivity of a metal covering intermediate to dynamic loading conditions. The methodology uses the dynamic split Hopkinson pressure bar (SHPB) test for measuring mechanical responses at medium strain rates by optimizing temperature increase, non-uniform strain rate distributed in the non-standard notched SHPB specimens. From the standard dynamic SHPB test, the thermal softening index of the Johnson–Cook (JC) model is first determined by fitting the FE simulation to temperature changes in the specimen. The discrepancy between the measured and predicted flow stresses with the conventional JC model can be attributed to the assumption of constant strain rate sensitivity. Therefore, the new approach using the notched SHPB specimens under dynamic loadings is introduced to identify mechanical responses covering a broader range of strain rate. Finally, the strain rate sensitivity parameter in the JC model as a function of strain rate is evaluated through the inverse FE scheme, in which the sigmoidal function is determined to be optimum by predicting the flow stresses under wider range of strain rate, especially in the intermediate range of strain rate. The present study provides a new methodology based on hybrid experiment and numerical simulation to fill the gap in predicting mechanical responses between quasi-static and dynamic tests using commonly available tensile test and SHPB test.

Keywords Split Hopkinson Pressure Bar test · Modified Johnson–Cook model · Strain rate · Inverse identification · Finite element simulation

1 Introduction

Accurate prediction of the deformation of structural materials under external mechanical loading is important to ensure structural integrity and optimal product performance. Failure in such prediction often leads to catastrophic structural collapses and functional deficiencies [1]. Particularly, the needs for the modeling of structure deformation subjected to high-speed impacts have gained considerable attentions [2]. In parallel with experimental studies, the design concepts based on modeling and simulation enable to reduce the material waste and to increase the efficiency for safety measures. This shift from experimental to numerical approach for optimizing the structure design under complex deformation mode enables the pursuit of economic and environmental benefits by minimizing cost and shortening construction timelines [3].

To effectively measure material properties under varying strain rate conditions, various experimental methods have been developed and employed, which is summarized in Fig. 1. For example, creep experiments, which observe deformation over time under a constant load, are utilized for the strain rates of 10^{-5}/s or lower [4–6]. Quasi-static strain rates up to 10^{-1}/s predominantly employ the equipment operated with hydraulic. Intermediate strain rates in the order of 10^{2}/s utilize the test machine for the high-speed hydraulic pressure application. For the dynamic strain rate

Yeong-Min Jeong and Seojun Hong have equally contributed to this manuscript.

✉ Myoung-Gyu Lee
myounglee@snu.ac.kr

[1] Department of Materials Science and Engineering and RIAM, Seoul National University, Seoul 08826, Republic of Korea

[2] Korea Army Academy at Yeongcheon, P.O.Box 135-1, Yeongcheon 38900, Republic of Korea

[3] Korea Institute of Materials Science, Changwon 51508, Republic of Korea

Published online: 28 February 2024

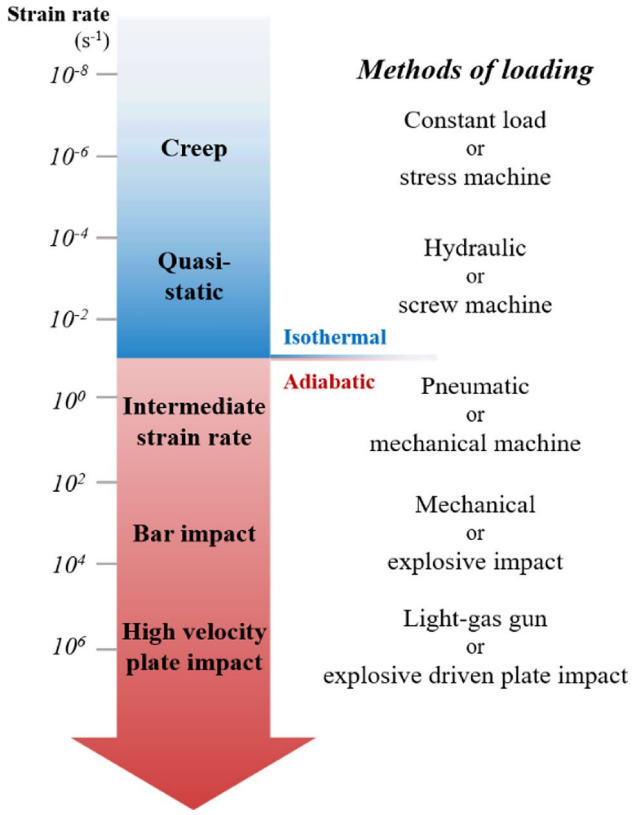

Fig. 1 Classification of experiments with respect to the value of strain rates

beyond the intermediate strain rate, the Split Hopkinson Pressure Bar (SHPB) test has been the primary experimental method employed to measure the stress–strain relationship over the strain rate 10^3/s [7–11]. Beyond this high-speed range, impact experiments involve gas guns or explosives [12–14]. These diverse experimental methods enable the comprehensive study of material properties across a wide range of strain rates.

Simultaneously with the advancement of experimental methods for measuring physical properties, methodologies for predicting the behavior of materials based on modeling have also been developed [15, 16]. Accurate expression of the physical properties of a material through constitutive equations is crucial for predicting material behavior. Consequently, as experimental methods have progressed, the development of constitutive equations to elucidate material behavior has also ensued [17–20]. In terms of the mechanical responses represented by the stress–strain relationship, the capability of predicting quasi-static deformation using constitutive equations has been quite satisfactory. However, various limitations from the aspects of both experiment and constitutive modeling have been reported in literature when it comes to predicting deformation under high strain rates and non-isothermal conditions [21].

To predict the mechanical properties of materials subjected to the high-speed deformation, researchers have undertaken studies on various dynamic constitutive equations. The examples of dynamic constitutive equations include the Johnson–Cook model, the Zerilli-Armstrong model, the Rusinek-Klepaczko model, and the Preston-Tonks-Wallace model [22–25]. Among these models, the Johnson–Cook (JC) hardening model has been widely recognized for its capability to accurately predict the plastic behavior of metallic materials across a broad range of strain, strain rate, and temperature conditions [26–28]. The JC hardening model is expressed as follows.

$$\overline{\sigma} = \left[A + B\left(\overline{\varepsilon}^{p}\right)^{n}\right]\left[1 + C\ln\left(\frac{\dot{\varepsilon}}{\dot{\varepsilon}_0}\right)\right]\left[1 - \left(\frac{T - T_0}{T_m - T_0}\right)^{m}\right] \tag{1}$$

where $\overline{\sigma}$, $\overline{\varepsilon}^{p}$, $\dot{\varepsilon}$, T are the equivalent stress, equivalent plastic strain, strain rate, and temperature, respectively. There are eight material constants $A, B, C, n, m, \dot{\varepsilon_0}, T_m, T_0$. Among them, $\dot{\varepsilon}_0, T_m, T_0$ are defined by reference data used in experiments, so that five parameters are additionally identified through the best fitting method in general. The three terms in square brackets represent the work hardening, strain rate sensitivity, and thermal softening, respectively.

As numerous efforts have been made to extend the applicability of the JC hardening model in predicting material behavior under a wide range of boundary conditions, significant concerns have emerged regarding the accuracy of the predicted results. Consequently, researchers have proposed various modified versions of the JC hardening model in different ways. In many instances, modifications were introduced to the work hardening and strain rate hardening terms, aiming to enhance the precision of predictions under plastic deformation of metallic materials [29–33]. Additionally, in some cases, adjustments were made to the heat softening term by incorporating conditions that specifically consider the temperature causing the recovery and/or recrystallization [34].

Many existing studies focusing on modifying the JC model often overlook the consideration of strain rates covering all ranges of strain rates from the quasi-static to high strain rate condition. While the quasi-static and high-speed deformation can be experimentally investigated through the quasi-static test and SHPB test, respectively, designing experiments for intermediate-speed deformation poses challenge. The manufacturing of relatively large-sized specimens required for intermediate-speed experiments is difficult, and even if such experiments are conducted, the tolerance is typically large, making it challenging to accurately determine the material properties. Additionally, special equipment for testing material properties under intermediate strain rates is not very common in both industry and academia.

In this study, we propose a new method that combines experimental data and finite element analysis (FEA) to determine the accurate JC parameters specifically under intermediate strain rate condition using the SHPB test. By utilizing the experimental data obtained from the SHPB test and employing the FEA technique, we can analyze the material properties in the intermediate strain rate range. This approach allows us to overcome the limitations associated with conducting experiments solely in the intermediate-speed range. Furthermore, we introduce a method to measure the thermal softening index of the material solely at room temperature, which traditionally requires experiments at various temperatures. This novel approach enables the determination of the thermal softening index through experiments conducted under a single temperature condition, simplifying the experimental procedure, and reducing the complexity of data analysis. By combining these approaches, we aim to provide a comprehensive and accurate characterization of material behavior under intermediate strain rate.

2 Split Hopkinson Pressure Bar (SHPB) Test: An Overview

The Split Hopkinson Pressure Bar (SHPB) experiment, initially developed by Hopkinson in 1914, has been widely utilized for measuring the high-speed mechanical properties of structural materials. This technique enables the realization of various strain rates, making it applicable in diverse fields. By adjusting the weight and firing velocity of the striker bar, the SHPB test can be performed to cover a broad range of strain rate. Moreover, the simplicity and versatility of the experimental setup allows for efficient numerical modeling using FE method. Therefore, this facilitates the prediction of material behavior with novel inverse approach employed in the present study, which will be further explained in detail.

The experimental setup of the SHPB experiment is illustrated in Fig. 2a, where a gas gun propels the striker bar, leading to its collision with the incident bar and subsequent energy transfer. This energy is propagated through a specimen and transmitted bar in the form of elastic waves. The strain gauge attached to each bar records the incident, reflected, and transmitted wave as the strain signal over time, providing visual representation on an oscilloscope. The shapes of the elastic waves are depicted in Fig. 2b. By analyzing these waves, it becomes feasible to calculate the displacement of the incident bar and transmitted bar, as well as the applied force on each bar. To determine the stress and strain imposed on the specimen, factors such as the cross-sectional area and Young's modulus of the bars, along with the cross-sectional area of the specimen, are taken into account. The SHPB experiment adheres to this overarching framework, enabling the estimation of stress and strain on the specimen by incorporating relevant parameters and measurements derived from the incident, reflected, and transmitted waves.

The stress and strain experienced by the specimen in the SHPB test are determined by analyzing the displacements of the incident and transmitted bars. Based on the principles of one-dimensional elastic wave propagation theory [35], the displacement u of the material can be calculated using Eq. (2), where c represents the propagation speed of the elastic wave.

$$u = c\int_0^t \varepsilon dt \tag{2}$$

The displacement of the incident bar, denoted as u_1, can be obtained by subtracting the displacement caused by the incident strain wave, ε_i, from the displacement caused by the reflected strain wave, ε_r. This relationship is mathematically represented by Eq. (3).

$$u_1 = c\int_0^t \left(\varepsilon_i - \varepsilon_r\right)dt \tag{3}$$

The displacement of the transmitted bar, u_2 can be expressed based on the output strain wave, as demonstrated by Eq. (4).

$$u_2 = c\int_0^t \varepsilon_t dt \tag{4}$$

If there is close contact between the specimen and each rod during deformation, the displacement of the specimen, denoted as u_s, can be expressed by subtracting the displacement of the incident bar from the displacement of the transmitted bar, as shown in Eq. (5).

$$u_s = u_1 - u_2 \tag{5}$$

From the Eq. (5), the strain ε_S of the specimen can be calculated as in Eq. (6).

$$\varepsilon_s = \frac{u_s}{l_0} = \frac{u_1 - u_2}{l_0} = \frac{c}{l_0}\int_0^t \left(\varepsilon_i - \varepsilon_r - \varepsilon_t\right)dt \tag{6}$$

The force applied on both sides of the specimen can be calculated as F_1 and F_2. These forces can be calculated using the equations provided in Eqs. (7) and (8).

$$F_1 = E_b A_b\left(\varepsilon_i + \varepsilon_r\right) \tag{7}$$

$$F_2 = E_b A_b \varepsilon_t \tag{8}$$

where E_b represents Young's modulus of the incident bar and the transmitted bar, and A_b and A_s denotes the cross-sectional areas of the bar and specimen, respectively.

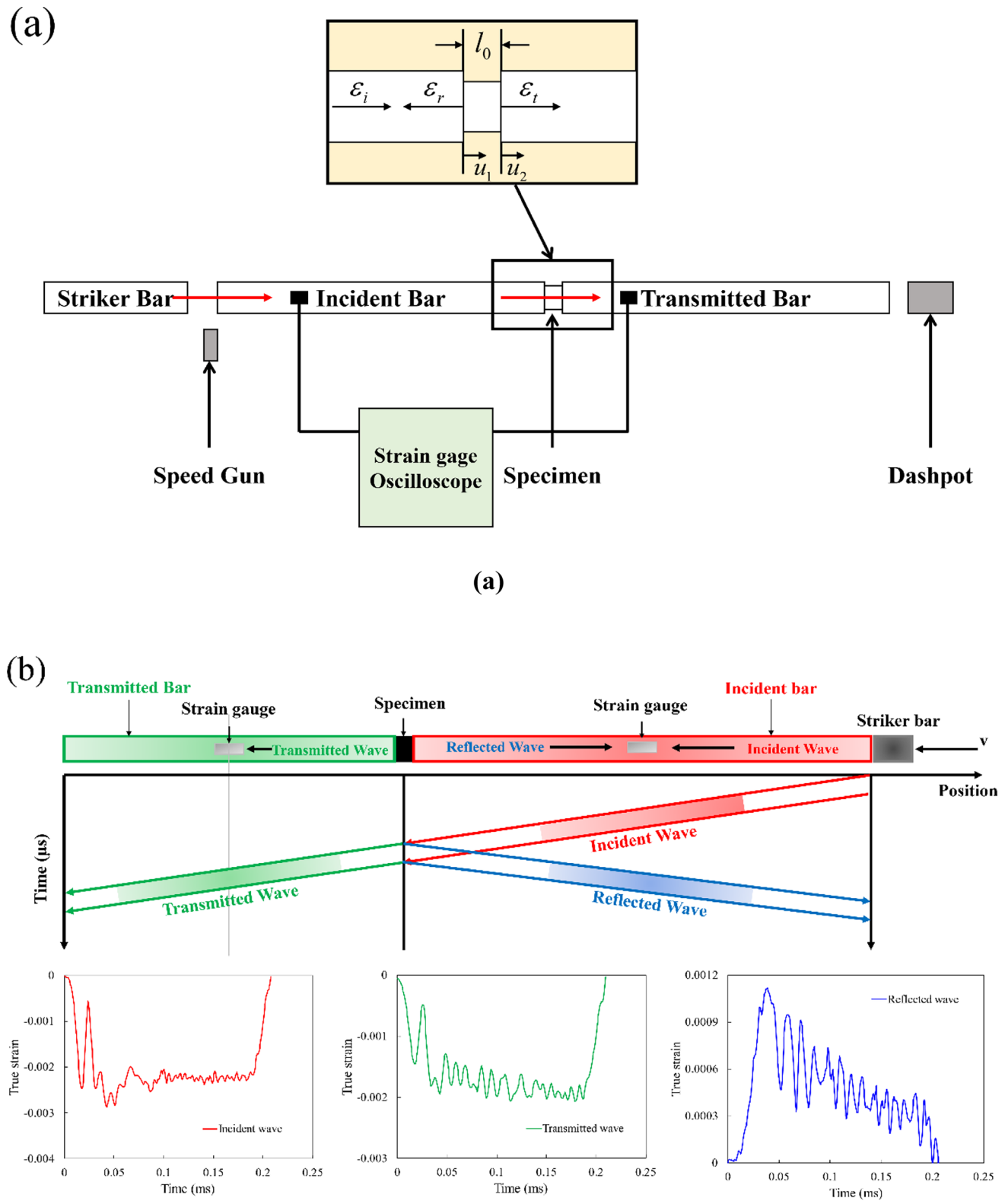

Fig. 2 **a** Schematic illustration of SHPB test, and **b** the elastic waves emitted during the tests

Therefore, the stress σ_s applied to the specimen is calculated as follows in Eq. (9).

$$\sigma_s = \frac{F_1 - F_2}{2A_s} = \frac{E_b A_b \left(\varepsilon_i + \varepsilon_r + \varepsilon_t\right)}{2A_s} \tag{9}$$

If the length l_0 of the specimen is sufficiently small, the calculation of stress and strain can be simplified by making the following assumptions, as shown in Eqs. (10), (11) and (12).

$$\varepsilon_r = \varepsilon_t - \varepsilon_i \tag{10}$$

$$\varepsilon_s = -\frac{2c}{l_0}\int_0^t \varepsilon_r dt \tag{11}$$

$$\sigma_s = \frac{E_b A_b \varepsilon_t}{A_s} \tag{12}$$

The validity of the assumptions has been established for specimens with a length of less than 3/4 inch [36]. To determine the strain rate, the strain of the specimen obtained through the procedure is divided by the time taken for deformation. Both the stress and strain of the specimen calculated using this method are engineering stress and engineering strain, respectively, in the direction of deformation. In many cases, the JC hardening model is optimized based on the true stress-true strain curve derived from the engineering stress. However, in compression experiments, there is a certain level of discrepancy between the measured true stress and the equivalent stress of the specimen due to frictional effects. Therefore, it is necessary to consider the influence of friction in the SHPB experiment [37], which will be discussed in the later section.

3 Experiments

3.1 Material

The material investigated in this study was a hot rolled steel. All testing samples were taken from the hot rolled H-beam. The material was manufactured by multi-pass hot rolling and quenching. The composition of the material is provided in Table 1.

3.2 Quasi-Static Tensile Test

A miniature tensile specimen was fabricated to conduct a quasi-static tensile test. The experiment was conducted using the Instron 5942 test equipment at the strain rates of 0.001 s^{-1}, 0.01 s^{-1}, and 0.1 s^{-1}. Specimen geometry and experimental setup are illustrated in Fig. 3a and b, respectively. Note that the specimen size was preliminary optimized to produce the strain rate up to 0.1 s^{-1} in the given testing equipment because the standard tensile test specimens cannot provide the strain rate near 0.1 s^{-1} in the current testing machine. A digital image correlation (DIC) technique with a commercial DIC software VIC-3D 7 was used to measure the strain during the test as an alternative to the common mechanical extensometer [38–40].

Table 1 Chemical compositions of the hot-rolled steel

Composition (wt%)										
C	Si	Mn	P	S	T/Al	Ni	V	Nb	Ti	N
0.105	0.220	1.494	0.012	0.003	0.019	0.070	Added	Added	Added	≤ 5

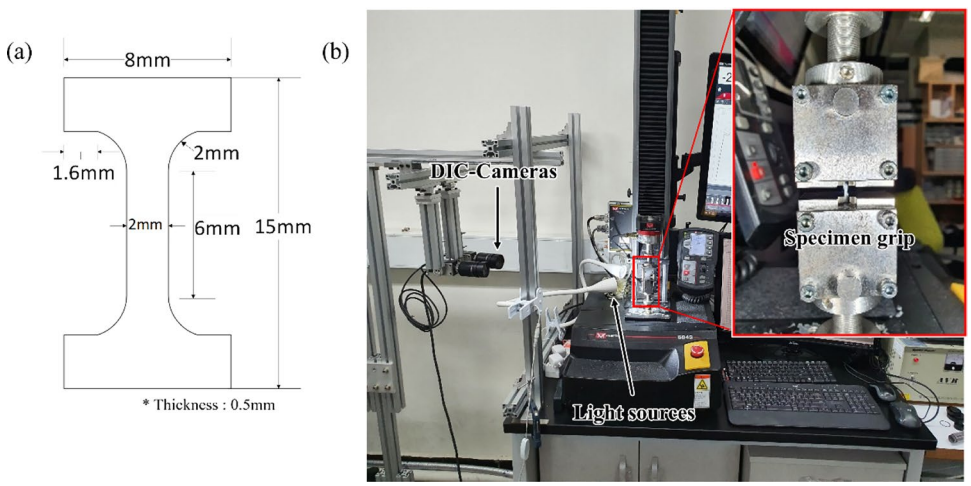

Fig. 3 **a** Miniature specimen geometry for tensile tests, and **b** DIC setup with the tensile testing machine

3.3 SHPB Compression Test with Non-Conventional Specimens

The SHPB experiments were performed at different speeds to examine the material properties under higher strain rate than the quasi-static test. Besides the mechanical properties, temperature data within the specimen during high-speed deformation were also collected using a K-type thermocouple. The experimental setup, depicted in Fig. 4a, encompassed the entire experimental environment. The specimen geometry used in the experiments varied for different SHPB test types, namely "Specimens 1–6", as illustrated in Fig. 4b–g. For the specimens 3–6, each cross-sectional geometry is shown in the right of each figure. The rationale behind conducting these diverse types of tests is elaborated in Sect. 5 of the study.

To achieve the various strain rates in the specimens, different test speeds were applied for the specimen geometries in Fig. 4b–g. The experimental setup and the velocity of the striker bar are summarized in Table 2. Similar to the quasi-static experiment, at least five tests were conducted for each test condition to ensure reproducibility of the results. The stress-strain curves were determined based on three sets of experiment data exhibiting high consistency. Note that the strain rate in Table 2 was calculated from the averaged total strain attained during the test.

In the SHPB test, the specimen deformation is also affected by the friction between the workpiece and incident bar. Therefore, proper lubricants have been applied to the contact surface such as the liquid type of lubricant at low temperature as well as gel or solid lubricants at high temperatures [41]. If the friction is not well controlled during the SHPB test, undesired specimen rotation occurs during deformation, which reduces the accuracy of the measurement. In this study, the Vaseline lubricant with a gel state was applied to achieve reliable and uniform friction during the test, which prevented the specimen rotation.

Table 2 SHPB test conditions

Name	Averaged strain rate (/s)	Length of striker bar (mm), Diameter = 19 mm	Impact speed (m/s)
Specimen-1	1000	456	21.5
	1400	456	26.3
	2000	304	30
Specimen-2	1000	456	21.5
	1400	456	26.3
	2000	304	30
Specimen-3	820	304	30
Specimen-4	530	304	30
Specimen-5	200	304	30
Specimen-6	570	304	30

4 Numerical Simulation and JC Parameter Optimization Procedure

In this study, the dynamic explicit FE software ABAQUS/Explicit was used for modeling the SHPB test. For the efficient control of computational cost, the optimized mass scaling factor of 100 was used. The main purpose of FE simulation is to accurately determine the coefficients of the JC hardening law by fitting the results obtained from SHPB experiments.

The FE model for the SHPB test and a flow chart summarizing the optimization process for the JC hardening parameters are shown in Fig. 5a and b, respectively. The initial estimation of JC hardening parameters was provided from the stress–strain data of quasi-static tensile test. Note

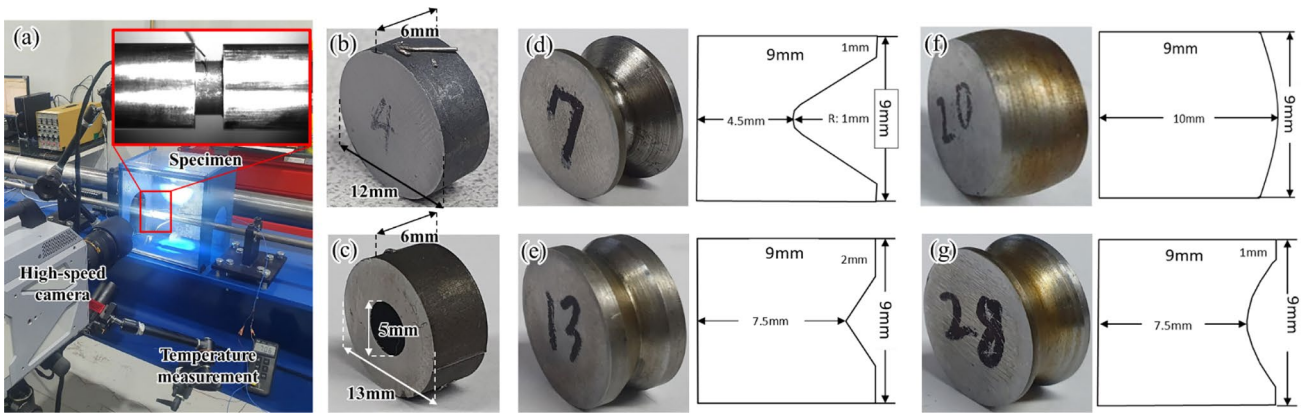

Fig. 4 **a** Experimental setup of the SHPB (red box indicates the position of incident bar, transmitted bar, and specimen in SHPB test). Specimen geometries **b**–**g** with different strain rates

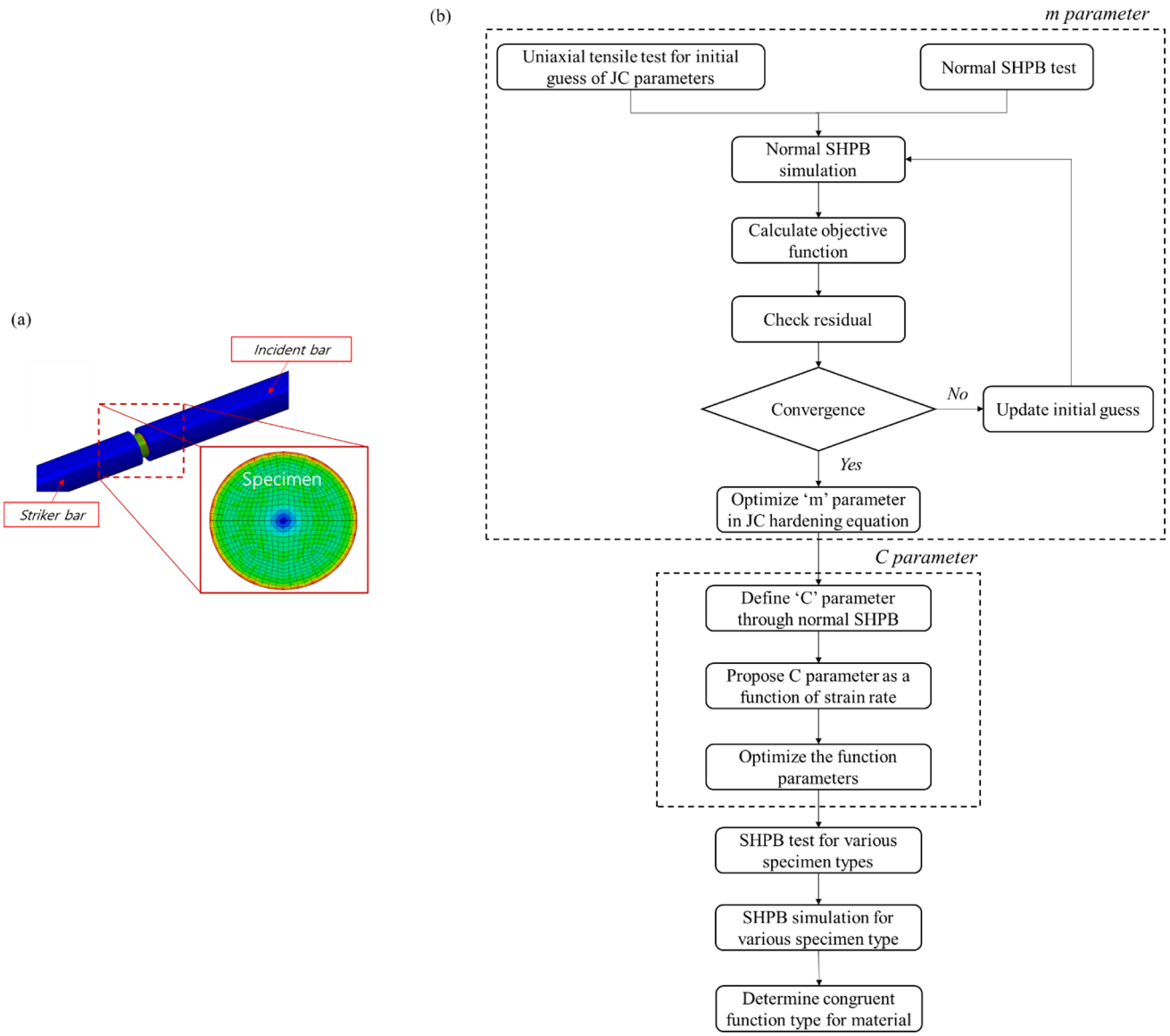

Fig. 5 **a** FE modeling for the SHPB test, and **b** flowchart of optimization procedure for the JC model parameters

that the initial guess from the quasi-static loading conditions cannot cover the high strain rate ranges. To incorporate the JC hardening in the FE analysis, a user-defined subroutine for hardening law, VUHARD in ABAQUS was coded. The workpiece was discretized with the 3D coupled thermo-mechanical continuum element C3D8T, and the number of elements and nodes were provided in Table 3. Note that mesh of Specimen-2 was more fine than other specimen types due to investigate the influence of friction effect. The workpiece specimen was assumed to be elastic–plastic material with von Mises isotropic yield function, while the incipient and striking bars were considered as isotropic linear elastic material. The coefficient of friction was assumed to be 0.1 during the SHPB test considering the commonly reported friction coefficient under lubrication.

Table 3 The number of element and nodes for various specimen types

Specimen type	Number of elements	Number of nodes
Specimen-1	3120	3360
Specimen-2	21,600	24,960
Specimen-3	3360	3926
Specimen-4	2244	2560
Specimen-5	2156	2472
Specimen-6	4424	4938

The combination of experiment and numerical simulation allowed for the refinement and optimization of the JC model parameters, enhancing the accuracy of the material behavior prediction.

Output variables from FE simulations, especially temperature and stress–strain curve, were evaluated to determine the convergence of optimization using the following objective function Ω.

$$\Omega = \sum_{t=1}^{T} \left(\frac{\left| \sigma_{\exp}^{(t)} - \sigma_{sim}^{(t)} \right|}{\sigma_{\exp}^{(t)}} \right) + \frac{\left| T_{\exp} - T_{sim} \right|}{T_{\exp}} \tag{13}$$

The objective function is based on both stress (σ) at the prescribed time steps, and temperature (T) between simulation (sim.) and experiment (exp). Temperature was measured at the end of testing. During the optimization process, the residual was calculated at each iteration through the evaluation of the objective function. If the residual did not meet the desired tolerance, the guess was modified, and the entire procedure was iterated using the Levenberg–Marquardt optimization algorithm implemented in MATLAB. This optimization approach, known as finite element model updating (FEMU), is widely recognized in the field of inverse methods [42]. Following the completion of the optimization procedure, the JC model parameters were successfully optimized, leading to the attainment of an optimized set of parameters for accurate material behavior prediction.

5 Results and Discussion

5.1 JC Hardening for Quasi-Static Loading Condition

From the tensile tests under quasi-static condition, the yield stress of the material was determined to be 427 MPa at the strain rate of 0.001 s^{-1}. By fitting the stress–strain curves under three different strain rates, the JC hardening constants B, n, and C in Eq. (1) were determined to be 657.8 MPa, 0.6894, and 0.009, respectively. In the model, the reference and melting temperatures T_r and T_m are referred to be 23 °C and 1538 °C, respectively. The comparisons between experiments and optimized JC hardening curves are shown in Fig. 6. The Fig. clearly shows that the measured flow stress curves between the strain rate 0.001 s^{-1} and 0.1 s^{-1} can be perfectly fitted to the measurable strains. In the quasi-static experiment conducted at room temperature, the temperature change of the specimen was virtually negligible during plastic deformation. Therefore, the coefficient m in Eq. (1), which represents the thermal softening by plastically dissipated heat generation, could be ignored by assuming the

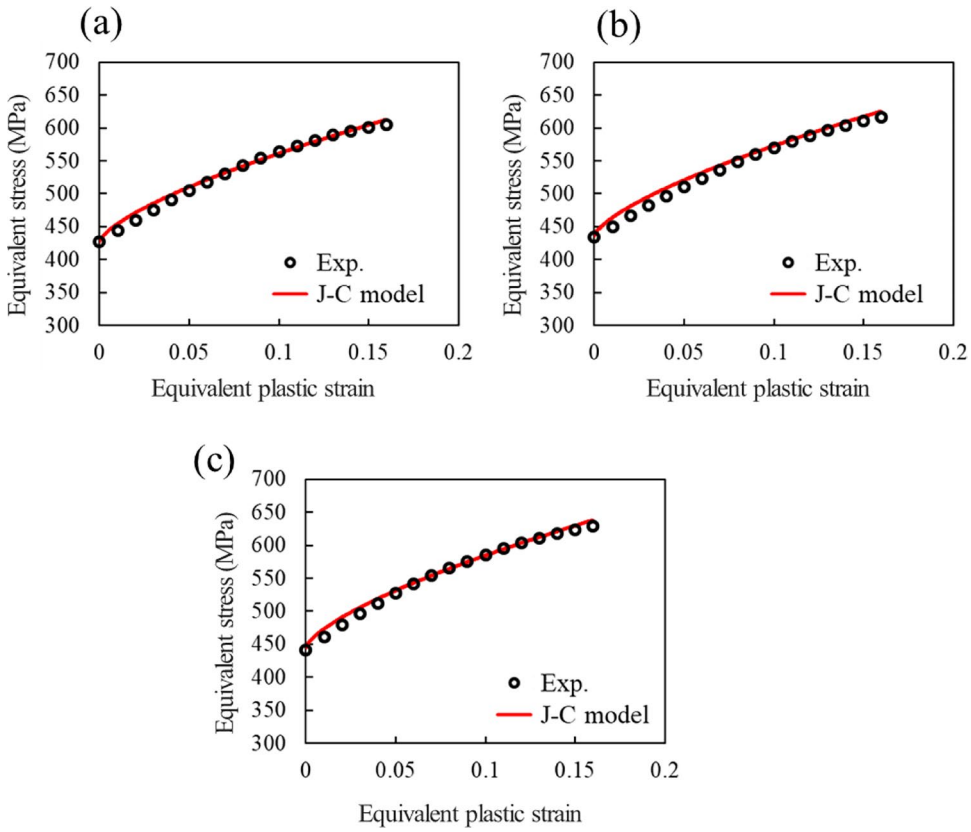

Fig. 6 Comparison between experiments and JC hardening fitted flow stress curves under quasi-static loading with the strain rate of **a** 0.001 s^{-1} **b** 0.01 s^{-1} **c** 0.1 $s.^{-1}$

isothermal condition for the JC modeling under quasi-static conditions. In the later section, a methodology for determining the thermal softening constant under high strain rates will be discussed.

5.2 SHPB Experiments and Simulations

Figure 7a shows the raw results for SHPB test using specimen-1 which reveals the repeatability at least 5 times. As shown in graph, there are large fluctuations in strain range 0–0.07. These large fluctuations are bound to be caused by experimental methodology and have been reported in other studies [9, 34, 37]. In this study, true stress–strain curves in strain over 0.7 is used for comparison and fitting. It is reasonable because this study focusses on the hardening curve rather than the yield stress. Over the strain value 0.7, the average true stress–strain curve is calculated and smoothened by MATLAB as shown in Fig. 7b

Figure 8 shows the comparison between the SHPB measured flow stress and the JC hardening fitted curves with coefficients based on the pre-determined quasi-static experiments. The three very high strain rates of 1000, 1400, and 2000s^{-1} were considered. In this case, the thermal softening parameter m was assumed to be 1.0 to consider the plastically dissipated heat generation at very short deformation time. The three figures clarify that the JC parameters identified from the low strain rates cannot be applied to predict the plastic behavior

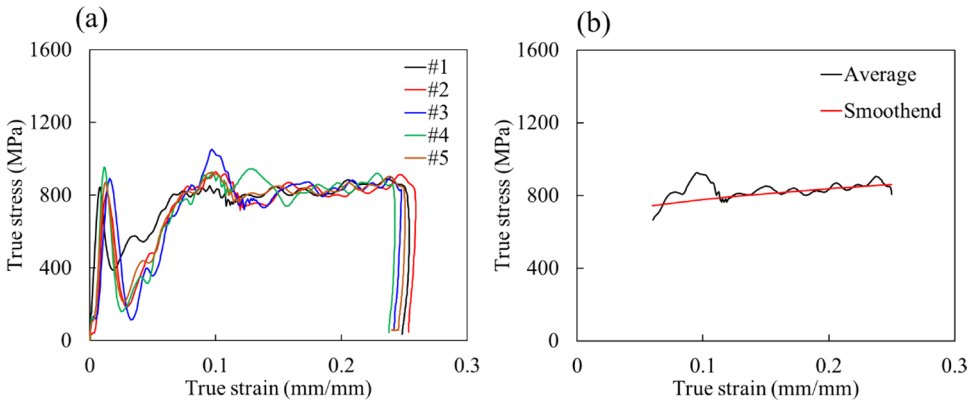

Fig. 7 **a** Raw data for true stress–strain curves using specimen-1 **b** Average true stress–strain curve and smoothened curve using MATLAB

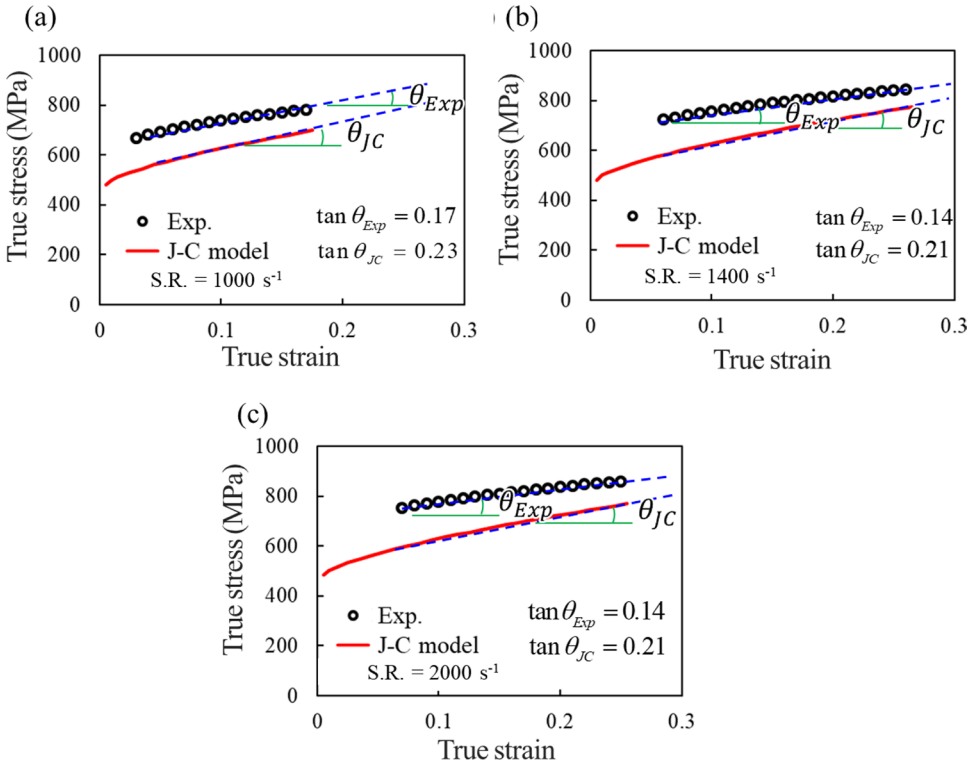

Fig. 8 Comparison between SHPB measured flow stress curves and J-C hardening curves with coefficient fitted to the quasi-static experiments. **a** Strain rate of 1000 s^{-1}, **b** 1400 s^{-1}, and **c** 2000s^{-1}

of the same material at much higher strain rate range. Especially, when the slope of hardening (represented in Fig. 8) is significantly deviated between the experiment and calculated JC flow curve. Note that the slope was measured by linear fitting of stress between the strain of 0.1 and 0.2 for both experiment and JC model. The slopes of measured flow stress at three high strain rates were 0.14–0.17(MPa), while those of the JC fitted with quasi-static flow curves were 0.21–0.23 MPa. The slope of the measured curves at high strain rates are much less than those of the quasi-static curves, which is attributed to the thermal softening effect caused by the temperature rise during the adiabatic process in high-speed deformation [43]. With these observations, the coefficient m in Eq. (1) was adjusted by conducting series of FE simulations until the measured temperature change can be well fitted. From this inverse identification procedure, the m value could be optimized as 0.69, which resulted in good agreement between measured and JC fitted slope of flow stress. The figures also show that the temperature rise after tests at three strain rates could be well fitted. The results highlight the significance of considering the thermal softening effect for improving the prediction of material behavior under high-speed deformation.

5.3 Analysis of JC Parameters Considering the Quasi-Static Behavior and Thermal Softening

The two main results of the previous sections can be summarized as follows: First, the JC hardening model can fit well the flow stresses for the strain rate variation under quasi-static level (Fig. 5). However, secondly, the flow stresses at high strain rates measured by SHPB test could not be reasonably predicted by the J–C model either with parameters identified from the quasi-static conditions (Fig. 8) or those from the SHPB results and temperature changes in the specimen (Fig. 9). In this section, the discrepancy between the model calculation and experiments in Fig. 9 is explained in terms of the friction effect and the dependency of hardening coefficient on strain rate. The hypothesis on friction is reasonable because the frictional force between the surfaces of specimen and elastic bars is inevitably involved during compression, which influences the stress–strain curve of the material during the SHPB tests [44]. Regarding the second hypothesis, the JC model in Eq. (1) has the coefficient for controlling the strain rate sensitivity C, which was assumed to be constant in the previous analysis. To relieve the constant condition, similar works reported the parameters as function of strain rate and/or temperature [29–33].

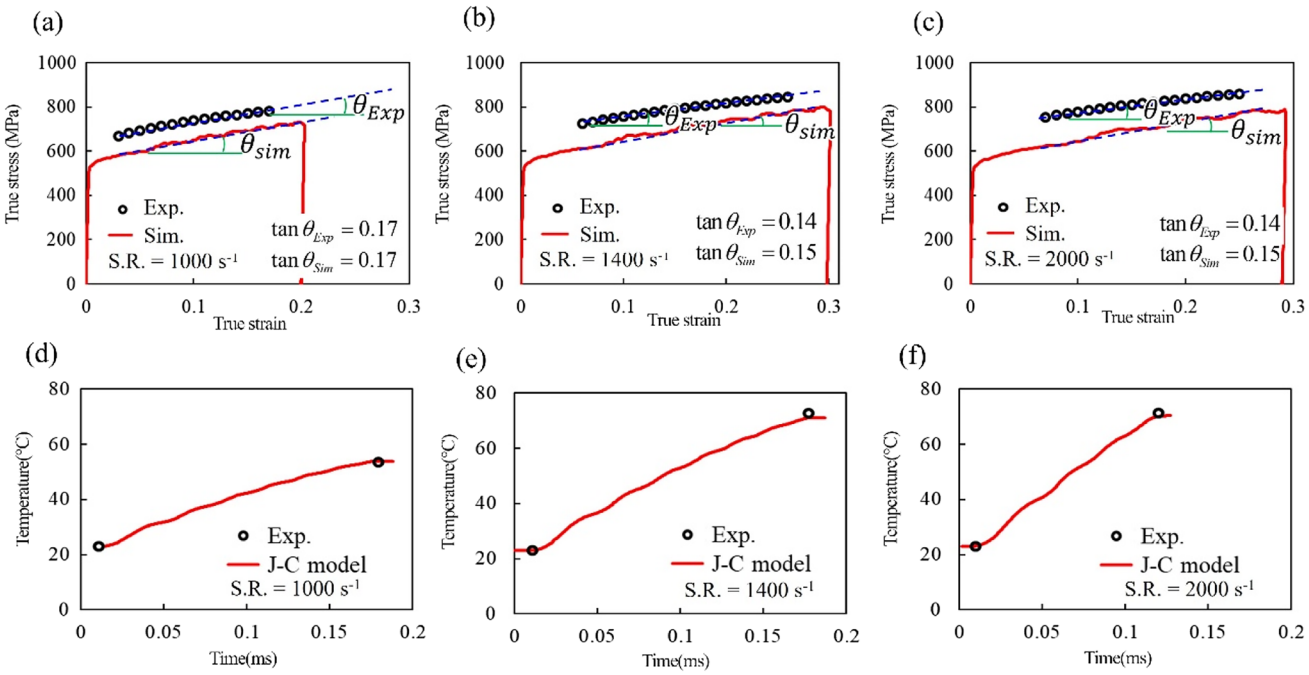

Fig. 9 Comparison of the SHPB measured flow stress and simulated flow curves with J–C model: **a** Strain rate of 1000 s^{-1}, **b** 1400 s^{-1}, and **c** 2000s^{-1}. The J–C model was fitted to both flow stresses and temperature changes **d–f** during deformation

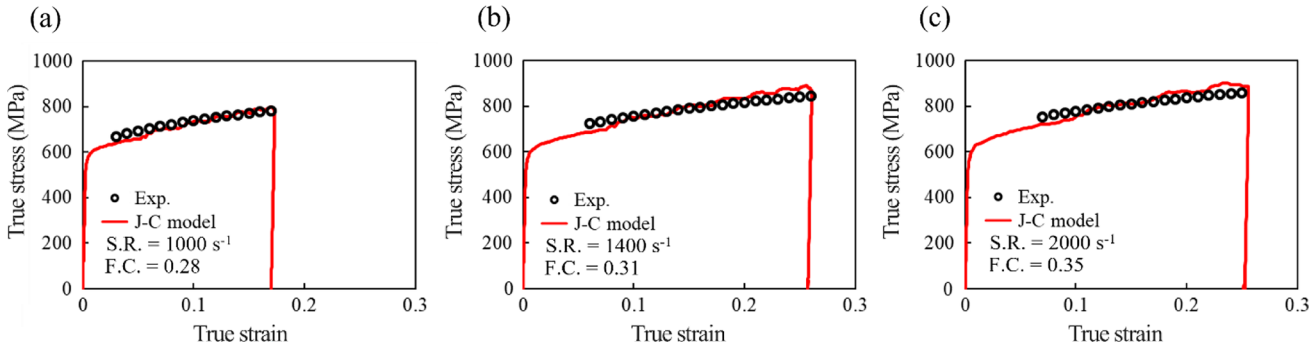

Fig. 10 The best fit flow stress curves calculated by finite element simulations with various friction coefficients for the strain rate of **a** 1000 s^{-1}, **b** 1400 s^{-1} and **c** 2000$s.^{-1}$

5.3.1 Effect of Friction on Flow Stress Curves

The effect of friction on the flow stress in SHPB test was further analyzed using the finite element simulation. As the first evaluation, the friction coefficients were iterated to fit the measured flow stresses under different strain rates. Figure 10 shows that the flow hardening curves could be well fitted with increased friction coefficients of 0.28 to 0.35 in the FE simulations. The difference in friction coefficient under pressure can be feasible from the previous study [44]. To validate if the friction coefficients to give best fit to the measured flow stresses in Fig. 10, the ring compression test was conducted to estimate the friction at the interface between the specimen and impact bar during SHPB [45, 46]. From the initial specimen geometry (Fig. 4c), the ring specimens were deformed after the SHPB tests as shown in Fig. 11a–c at the strain rates of 1000 s^{-1}, 1400 s^{-1}, and 2000s^{-1}, respectively. As illustrated in Fig. 11d, less sliding occurs at the interface for high friction, while low friction allows for simultaneous sliding at the interface leading to deformation with an increased inner diameter. From the measured change in specimen's inner diameter and the calibration curve in Fig. 11e [45, 46], the friction coefficient in the present investigation can be approximated to be 0.02 regardless of the strain rate. Compared to the best fitting friction coefficients determined from the FE simulations (in Fig. 10), it is reasonable to exclude the effect of friction on the flow stress curves measured by the current SHPB test.

5.3.2 Effect of Non-Constant Strain Rate Sensitivity on Flow Stresses

As a second hypothesis for a reason of discrepancy between the model prediction and experiment, the effect of strain rate sensitivity parameter C in the JC hardening model (Eq. (1)) is investigated. As can be seen in Fig. 12, model parameter C varies depending on the strain rate. For this, C was defined as a function of the averaged strain rate, which resulted in the best fitting to the measured flow stresses during SHPB tests. The results of FE simulations provided good agreements with experiments when the parameters C increased with respect to the strain rate in the investigated strain rate range.

The validity of the parameter C as a function of strain rate determined by fitting the flow stresses in quasi-static and dynamic strain rate condition is proved by designing a new experiment-simulation method as follows. First, the most appropriate function for the parameter C is constructed to cover the whole range of strain rate. This is because the current testing results only covered the quasi-static and high strain rate over 1000 /s and the data in the intermediate strain range are missing. Then, the new sample design is proposed so that the deformation in the SHPB test involves the wide range of strain rate simultaneously during the test. Therefore, if the proposed constitutive model with variable C parameter is rationale, the overall mechanical response should be well predicted.

Regarding the optimal function type of strain rate sensitivity parameter, three forms of equation based on the best fitted parameters in both quasi-static and dynamic conditions were tested: (1) the power-law of the logarithmic strain rate (C_1, Eq. 14), (2) the power-law of the strain rate (C_2, Eq. 15), and (3) the sigmoidal function of the logarithmic strain rate (C_3, Eq. (16)). These functions are intended similar fitting of the flow stresses in the measured range of strain rate, while they differ in the intermediate strain range. The three types of the functions and their model parameters are shown in Fig. 13 and Table 4, respectively.

$$C_1 = a_1 \times \left(\ln \left(\frac{\dot{\varepsilon}}{\dot{\varepsilon}_0} \right) \right)^{b_1} + c_1 \tag{14}$$

$$C_2 = a_2 \times \left(\frac{\dot{\varepsilon}}{\dot{\varepsilon}_0} \right)^{b_2} + c_2 \tag{15}$$

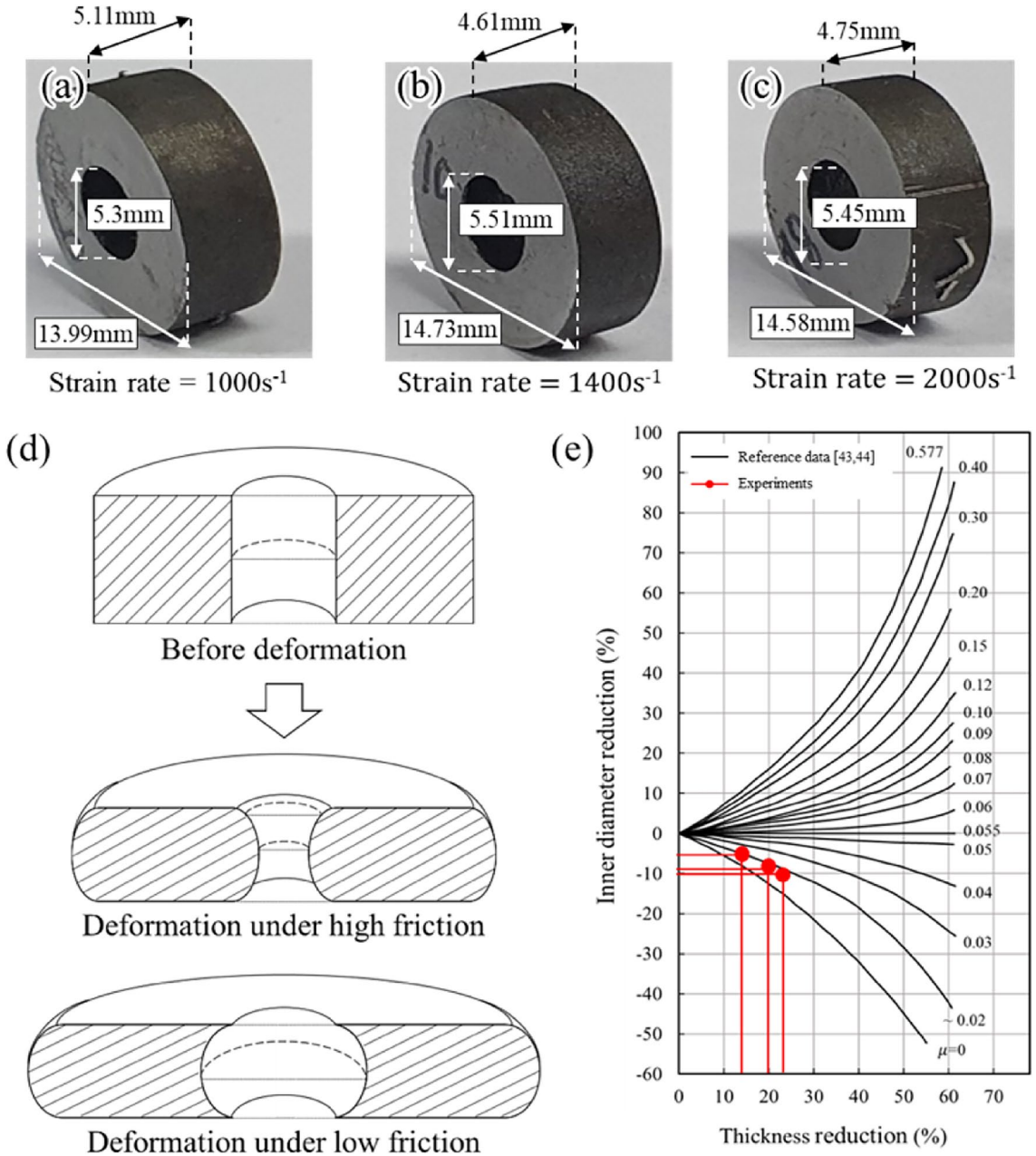

Fig. 11 Deformed specimens after ring SHPB test under different strain rates: **a** 1000 s^{-1}, **b** 1400 s^{-1} and **c** 2000$s.^{-1}$. **d** Schematics of deformed specimen shape after ring compression test and their relationship with friction coefficient. **e** Determination of friction coefficient from the ring SHPB tests using the reference calibration curve [45, 46]

$$C_3 = a_3 \times \arctan\left(b_3 \times \ln\left(\frac{\dot{\varepsilon}}{\dot{\varepsilon}_0}\right) + c_3\right)^{b_3} + d_3 \tag{16}$$

Then, the optimum C parameter in the JC model among Eqs. (14)–(16) were determined by conducting FE simulations and their comparison with experiments for non-standard test specimens which include the wider range of strain rate (especially from medium to high strain rate) in the specimen during common SHPB experiments. For this, the new design of specimens with varying cross-sectional area of the SHPB specimen by introducing different notches were proposed. The four specimens are denoted as "Specimen-3" to "Specimen-6", which are shown in Fig. 14a–d. From the preliminary FE simulations, the distribution of the strain rate on each specimen was pre-evaluated. As shown in Fig. 14e–h, each specimen represents

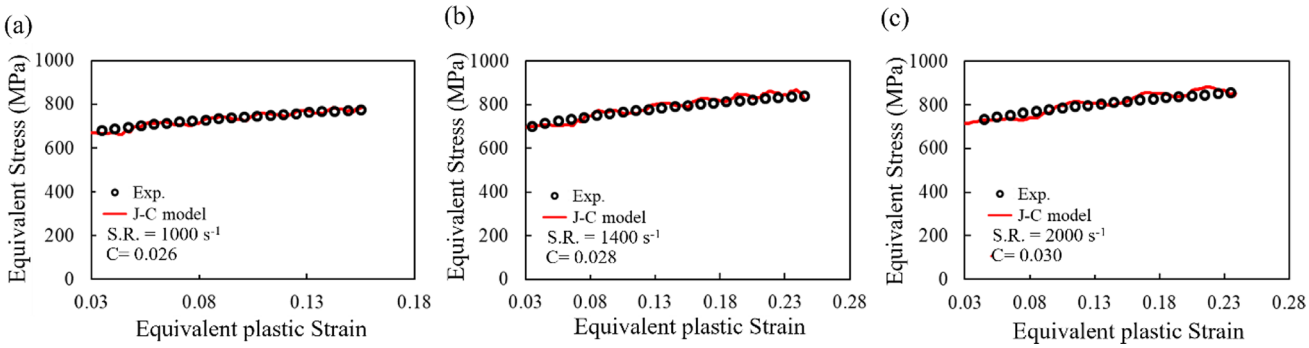

Fig. 12 Flow stress curves fitted to measured data using variable strain rate sensitivity parameter C in Eq. (1) as a function of three investigated strain rates: **a** 1000/s, **b** 1400/s, **c** 2000/s

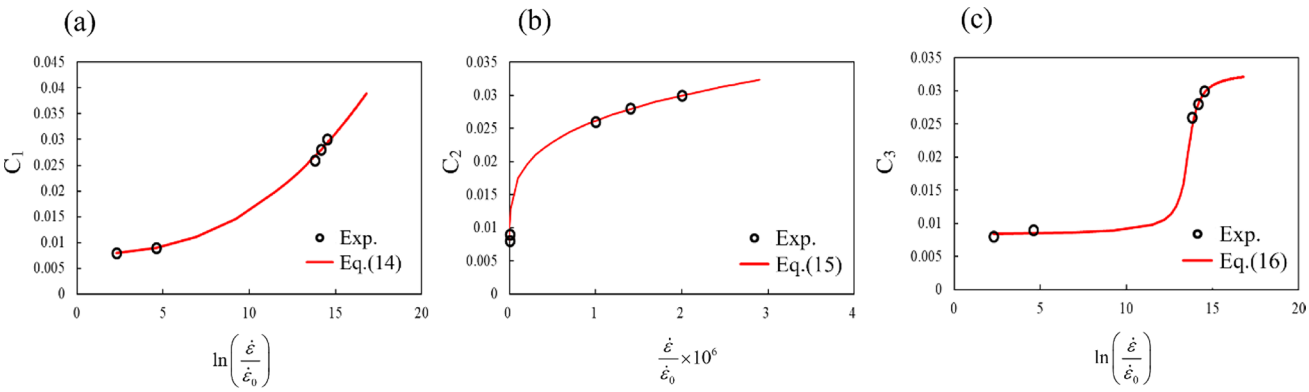

Fig. 13 The three types of C parameter (C_1, C_2, C_3) as a function of strain rate according to **a** Eq. (14), **b** Eq. (15), and **c** Eq. (16)

Table 4 The best fitting parameters of C_1, C_2, and C_3

	Hardening parameters			
C_1	a_1	b_1	c_1	d_1
	2.518×10^{-5}	2.524	7.754×10^{-3}	-
C_2	a_2	b_2	c_2	d_2
	4.918×10^{-4}	0.2643	7.206×10^{-3}	-
C_3	a_3	b_3	c_3	d_3
	7.966×10^{-3}	2.304	-31.31	2.066×10^{-3}

quite distinctive strain rate distribution under the same loading condition of SHPB test. For example, the Specimen-1 includes the bi-modal distribution of strain rate with two peaks at around 200/s and 1400/s.

Finally, the force–displacement curves of the four newly designed specimens were predicted by adopting the three different C parameters of the JC hardening model. Figure 15 shows the comparison between the FE calculated flow curves and experimental results. It is shown that all the three models fitted well the trend of flow curves, but the best agreement could be obtained for the strain rate coefficient with the sigmoidal type function C_3 in Eq. (16). The sigmoidal function is featured with no significant change in the intermediate-high strain rate range, but beyond a certain strain rate threshold the C parameter rapidly increases before being stabilized. Similar observations were also reported in other studies [31, 47], which proves the validity of the present inverse experimental–numerical approach.

6 Conclusions

This study proposed a new inverse approach for identifying wider range of strain rate sensitivity using the conventional SHPB experiments, especially at intermediate strain rate regime. The method includes characterization of quasi-static stress–strain curves using the standard tensile test and dynamic flow stresses based on the SHPB test. Then, the flow stresses in the medium range of strain rate are optimized through the finite element updating (FEMU) method on newly proposed non-standard notched SHPB specimens designed for including wider strain rate distributions. The main conclusions of the present study can be summarized as follows.

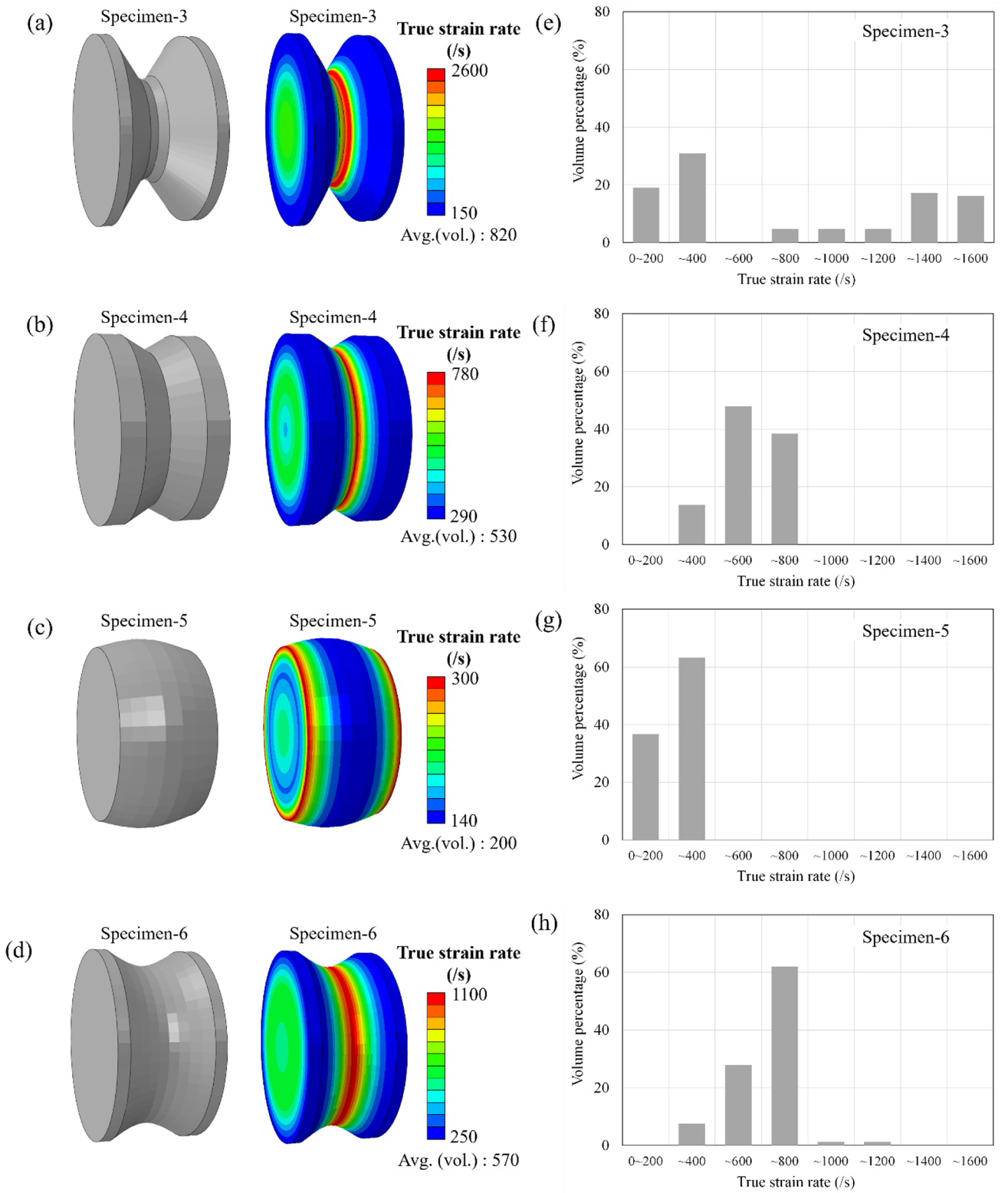

Fig. 14 **a–d** The newly designed SHPB specimens and **e–h** the distributions of strain rate in each specimen calculated by FE simulation

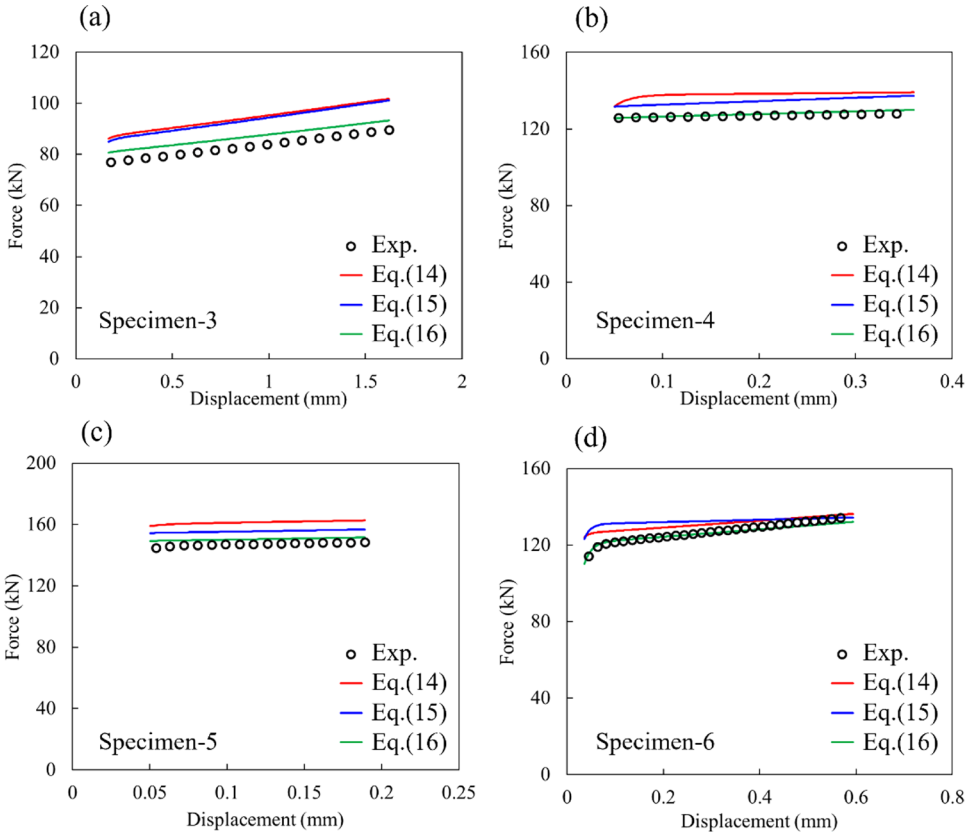

Fig. 15 FE calculated force–displacement curves for the four different specimen geometries in Fig. 14a–d and their comparison with measured curves. Three C parameter functions in Eqs. (14)–(16) were used for the simulations: **a** Specimen-1, **b** Specimen-2, **c** Specimen-3, and **d** Specimen-4

(1) The Johnson–Cook hardening model could be well fitted to the flow stresses between the strain rate of 10^{-3}/s and 10^{-1}/s measured by quasi-static tensile tests. In this range of strain rate, the effect of temperature increase from the plastic strain dissipation could be ignored.
(2) In the dynamic tests with standard SHPB specimens, the thermal softening index, m value in the JC hardening model, could be determined from fitting the finite element simulation to the measured temperature changes during adiabatic process of high-strain-rate tests. The inverse engineering approach through the iterative finite element updating scheme could be an efficient method for obtaining the thermal softening index as an alternative to the direct isothermal testing method.
(3) The effect of friction on the flow stresses measured by the SHPB tests was marginal, and the estimated friction coefficient using the conventional specimen with holes in the dynamic condition was less than 0.05 in this study.
(4) The discrepancy between the measured flow stress and the predicted one with the conventional JC hardening model can be attributed from the use of constant strain rate sensitivity parameter. Therefore, a new approach for determining the strain rate sensitivity parameter using the notched SHPB specimens was suggested. The new notched specimen design included the optimization of strain rate distribution in the specimens, where a broader range of strain rate could be attainable in a single specimen.
(5) The strain rate sensitivity parameter as a function of strain rate itself was evaluated for three different forms of function. Then, through the inverse FE scheme with the newly designed notched specimens of SHPB test, the sigmoidal function was found to be optimum by predicting the flow stresses under wider range of strain rate, especially in the intermediate range of strain rate.
(6) The present study provides a new methodology based on hybrid experiment and numerical simulation to fill the gap in predicting mechanical responses between quasi-static and dynamic tests using commonly available tensile test and SHPB test.

Acknowledgements This work was partially supported from KEIT (No.20010453) and from NRF of Korea (No. 2022R1A2C2009315). MGL also appreciates the support from the Institute of Engineering Research at Seoul National University.

Funding Open Access funding enabled and organized by Seoul National University.

Declarations

Conflict of interest The authors have no competing interests to declare that are relevant to the content of this article.

References

1. H. Yang, X. Wang, P. Ni, Z. Li, H. Liu, Met. Mater. Int. **28**, 1938–1947 (2022). https://doi.org/10.1007/s12540-021-01105-4
2. A. Abd El-Aty, Y. Xu, S.-H. Zhang, S. Ha, Y. Ma, D. Chen, J. Adv. Res. **18**, 19–37 (2019). https://doi.org/10.1016/j.jare.2019.01.012
3. J. Park, K.M. Min, H. Kim, S.H. Hong, M.G. Lee, Adv. Mater. Technol. **8**, 2201057 (2023). https://doi.org/10.1002/admt.202201057
4. M. Pec, H. Stünitz, R. Heilbronner, M. Drury, C. de Capitani, Earth Planet. Sci. Lett. **355–356**, 299–310 (2012). https://doi.org/10.1016/j.epsl.2012.09.004
5. E. Andrews, L.J. Gibson, M. Ashby, Acta Mater. **47**, 2853–2863 (1999). https://doi.org/10.1016/s1359-6454(99)00150-0
6. J.E. Dorn, J. Mech. Phys. Solids **3**, 85–116 (1955). https://doi.org/10.1016/0022-5096(55)90054-5
7. W. Chen, F. Lu, M. Cheng, Polym. Test. **21**, 113–121 (2002). https://doi.org/10.1016/s0142-9418(01)00055-1
8. A.S. Khan, Y.S. Suh, R. Kazmi, Int. J. Plast. **20**, 2233–2248 (2004). https://doi.org/10.1016/j.ijplas.2003.06.005
9. J. Kajberg, B. Wikman, Int. J. Solids Struct. **44**, 145–164 (2007). https://doi.org/10.1016/j.ijsolstr.2006.04.018
10. M. Tucker, M. Horstemeyer, W. Whittington, K. Solanki, P. Gullett, Mech. Mater. **42**, 895–907 (2010). https://doi.org/10.1016/j.mechmat.2010.07.003
11. A.S. Khan, M. Baig, S.-H. Choi, H.-S. Yang, X. Sun, Int. J. Plast. **30–31**, 1–17 (2012). https://doi.org/10.1016/j.ijplas.2011.08.004
12. R. Menikoff, J. Appl. Phys. **90**, 1754–1760 (2001). https://doi.org/10.1063/1.1385568
13. H. Jarmakani, J. McNaney, B. Kad, D. Orlikowski, J. Nguyen, M. Meyers, Mater. Sci. Eng. A **463**, 249–262 (2007). https://doi.org/10.1016/j.msea.2006.09.118
14. L. P. Martin, J. R. Patterson, D. Orlikowski and J. H. Nguyen, J. Appl. Phys. 1022007). https://doi.org/10.1063/1.2756058
15. J.S. Choi, J.W. Lee, J.-H. Kim, F. Barlat, M.G. Lee, D. Kim, Int. J. Mech. Sci. **98**, 144–156 (2015). https://doi.org/10.1016/j.ijmecsci.2015.04.014
16. K. Chung and M.-G. Lee, *Basics of Continuum Plasticity* (Springer, Singapore, 2018). https://doi.org/10.1007/978-981-10-8306-8
17. J. Bang, G. Bae, M. Kim, J. Song, M.-G. Lee, H.-G. Kim, Met. Mater. Int. **30**, 425–440 (2024). https://doi.org/10.1007/s12540-023-01524-5
18. J. Liao, X. Xue, M.-G. Lee, F. Barlat, G. Vincze, A.B. Pereira, Int. J. Plast. **93**, 64–88 (2017). https://doi.org/10.1016/j.ijplas.2017.02.009
19. H.-R. Lee, M.-G. Lee, N. Park, Met. Mater. Int. **28**, 2356–2370 (2022). https://doi.org/10.1007/s12540-022-01245-1
20. J. Bang, M. Kim, G. Bae, J. Song, H.-G. Kim, M.-G. Lee, Met. Mater. Int. **29**, 327–342 (2023). https://doi.org/10.1007/s12540-022-01244-2
21. P. Simon, Y. Demarty, A. Rusinek, G.Z. Voyiadjis, Metals **8**, 795 (2018). https://doi.org/10.3390/met8100795
22. G.R. Johnson, W.H. Cook, in *Proceedings of the of 7th International Symposium on Ballistics*. Hague, 19-21 April 1983 (American Defense Preparedness Association, 1983)
23. F.J. Zerilli, R.W. Armstrong, J. Appl. Phys. **61**, 1816–1825 (1987). https://doi.org/10.1063/1.338024
24. A. Rusinek, J. Klepaczko, Int. J. Plast. **17**, 87–115 (2001). https://doi.org/10.1016/s0749-6419(00)00020-6
25. D.L. Preston, D.L. Tonks, D.C. Wallace, J. Appl. Phys. **93**, 211–220 (2003). https://doi.org/10.1063/1.1524706
26. A. Shrot, M. Bäker, Comput. Mater. Sci. **52**, 298–304 (2012). https://doi.org/10.1016/j.commatsci.2011.07.035
27. X. Wang, J. Shi, Int. J. Impact Eng. **60**, 67–75 (2013). https://doi.org/10.1016/j.ijimpeng.2013.04.010
28. S.K. Dasari, S. Ganguly, A. Abutunis, K. Chandrashekhara, M.F. Buchely, S.N. Lekakh, R.J. O'Malley, T. Natarajan, Met. Mater. Int. **29**, 3340–3355 (2023). https://doi.org/10.1007/s12540-023-01442-6
29. Y. Lin, X.-M. Chen, G. Liu, Mater. Sci. Eng. A **527**, 6980–6986 (2010). https://doi.org/10.1016/j.msea.2010.07.061
30. X. Wang, C. Huang, B. Zou, H. Liu, H. Zhu, J. Wang, Mater. Sci. Eng. A **580**, 385–390 (2013). https://doi.org/10.1016/j.msea.2013.05.062
31. D.-N. Zhang, Q.-Q. Shangguan, C.-J. Xie, F. Liu, J. Alloys Compd. **619**, 186–194 (2015). https://doi.org/10.1016/j.jallcom.2014.09.002
32. B. Erice, C.C. Roth, D. Mohr, Mech. Mater. **116**, 11–32 (2018). https://doi.org/10.1016/j.mechmat.2017.07.020
33. Z. Liu, H. Zhao, J. Li, Z. Niu, V. Ji, J. Mater. Eng. Perfom. **32**, 4022–4030 (2023). https://doi.org/10.1007/s11665-022-07392-1
34. S. Seo, O. Min, H. Yang, Int. J. Impact Eng. **31**, 735–754 (2005). https://doi.org/10.1016/j.ijimpeng.2004.04.010
35. J.D. Achenbach, *Wave Propagation in Elastic Solids* (North Holland, Amsterdam, 1973). https://doi.org/10.1016/c2009-0-08707-8
36. U.S. Lindholm, J. Mech. Phys. Solids **12**, 317–335 (1964). https://doi.org/10.1016/0022-5096(64)90028-6
37. H. Meng, Q.M. Li, Int. J. Impact Eng. **28**, 537–555 (2003). https://doi.org/10.1016/s0734-743x(02)00073-8
38. N. McCormick, J. Lord, Mater. Today **13**, 52–54 (2010). https://doi.org/10.1016/s1369-7021(10)70235-2
39. B. Pan, Exp. Mech. **51**, 1223–1235 (2011). https://doi.org/10.1007/s11340-010-9418-3
40. C. Kim, H.J. Bong, K.S. Lee, M.-G. Lee, J. Lee, JOM **75**, 5494–5504 (2023). https://doi.org/10.1007/s11837-023-06146-1
41. M. Sarkar, N. Mandal, Mater. Today: Proc. **66**, 3762–3768 (2022). https://doi.org/10.1016/j.matpr.2022.06.030
42. J.Y. Won, S. Hong, B. Nam, J. Jung, Y. Kim, M.-G. Lee, JOM **75**, 5479–5493 (2023). https://doi.org/10.1007/s11837-023-06164-z
43. F. Siddique, F. Li, M.Z. Hussain, Q. Zhao, Q. Li, Met. Mater. Int. **29**, 3587–3606 (2023). https://doi.org/10.1007/s12540-023-01466-y
44. W. Zhong, A. Rusinek, T. Jankowiak, F. Abed, R. Bernier, G. Sutter, Tribol. Int. 90, 1–14 (2015). https://doi.org/10.1016/j.triboint.2015.04.002
45. T. Jankowiak, A. Rusinek, G. List, G. Sutter, F. Abed, Tribol. Int. **95**, 86–94 (2016). https://doi.org/10.1016/j.triboint.2015.10.039
46. A.T. Male, M. G.Cockcroft, J. Inst. Met. **93**, 38 (1964)
47. H. Sofuoglu, J. Rasty, Tribol. Int. **32**, 327–335 (1999). https://doi.org/10.1016/s0301-679x(99)00055-9

48. J.Q. Tan, M. Zhan, S. Liu, T. Huang, J. Guo, H. Yang, Mater. Sci. Eng. A **631**, 214–219 (2015). https://doi.org/10.1016/j.msea.2015.02.010